Journal of Metals, Materials and Minerals, 36(4), e2587, 2026

Mechanical behavior of porous Mg-10Zn bone scaffolds fabricated via low-temperature powder metallurgy

Nayyar Ijaz DAR[1], Donghui YANG[1,2,3,*], Zilong WANG[1], Bin WANG[1], and Wenkai WANG[3]

[1] Jiangsu Provincial Engineering Research Center for Structure-Function Integrated Metallic Materials for Harsh Environments, College of Materials Science and Engineering, Hohai University, Changzhou, 213200, China
[2] Innovation Center for Critical Materials in Hydraulic Infrastructure Safety and Water Environment Restoration, College of Materials Science and Engineering, Hohai University, Changzhou, 213200, China
[3] Suqian *Research Institute of Hohai University, Suqian, 223800, China*

***Corresponding author e-mail**: donghuiyang@hhu.edu.cn

Received date:
28 November 2025
Revised date:
21 May 2026
Accepted date:
23 June 2026

Keywords:
Powder metallurgy;
Porous magnesium scaffold;
Mg-Zn alloys;
Mechanical properties

Abstract

The development of bone scaffold materials must balance the conflict between high porosity for biological integration and sufficient mechanical strength to support physiological loads. This reasoning underpins the investigation of biodegradable magnesium alloys, which offer biocompatibility and a bone-like modulus to prevent stress-shielding. This study focuses on the low-temperature fabrication of a porous Mg-10 wt% Zn alloy scaffold via powder metallurgy route, with the purpose of rigorously characterizing its mechanical properties and establish a critical structure-property relationships fabricated for bone implant applications. Therefore, scaffolds with target porosities of 40%, 60%, and 70% were fabricated, with the resultant architectural analysis confirming achieved porosities of 40.65%, 60.38%, and 68.70%, respectively. Their mechanical performance was evaluated through Vickers microhardness measurements and uniaxial compressive testing. Interestingly, the microhardness of the scaffolds remained nearly constant at approximately 42.3 ± 3.0 HV, irrespective of porosity. Whereas, the compressive strength demonstrated a predictable decline with increasing porosity, from 20.11 ± 0.40 MPa to 3.81 ± 0.45 MPa. Crucially, all three scaffold variants exhibited compressive strength and elastic modulus values that fall within the documented range for human cancellous bone. The results demonstrate that low-temperature fabricated Mg-10 wt% Zn scaffolds provide tunable porosity and predictable mechanical performance, offering a basis for future investigations into their degradation behavior and biological response.

1. Introduction

Bone defects and dysfunctions arising from traumatic fractures, spinal degenerative diseases, and other pathologies represent a significant clinical challenge, driving extensive research into advanced bone repair materials and bone tissue engineering [1,2]. These materials are broadly categorized for cortical or cancellous bone applications. Cortical bone, found in the shafts, is dense and compact, whereas cancellous bone, located at the ends, possesses a porous, trabecular network that provides a large specific surface area, high porosity, and sufficient mechanical strength to maintain morphology and resist stress [3,4]. Common cancellous bone repair materials include bio-ceramics, polymers, and metals [5,6]. A paramount challenge in orthopedic surgery is the development of bone scaffolds that offer temporary mechanical support and subsequently degrade, being replaced by nascent bone tissue.

Magnesium (Mg) is a prominent candidate for biodegradable implants, primarily due to its biocompatibility and mechanical properties that closely match those of natural bone [7,8]. With a density of 1.738 $g \cdot cm^{-3}$ and an elastic modulus of 45 GPa, Mg mirrors the characteristics of human bone (density: 1.8 $g \cdot cm^{-3}$ to 2.1 $g \cdot cm^{-3}$, modulus: 40 GPa to 57 GPa). This congruence mitigates the risk of stress-shielding, a common issue with higher modulus implant materials like titanium [9]. Furthermore, Mg's inherent biodegradability in physiological environments obviates the need for secondary surgical removal.

The deployment of biodegradable magnesium alloys necessitates careful selection of alloying elements to ensure biosafety. Certain elements, such as copper and aluminum, are problematic due to their established toxicological profiles for instance, copper accumulation is implicated in neurodegenerative pathologies like Alzheimer's, while high doses of aluminum can induce estrogen-related gene expression in human breast cancer models [10]. In this context, zinc (Zn) distinguishes itself as a biocompatible alternative. Zn is not only well-tolerated but is also a physiologically essential micronutrient, serving as a cofactor for over 300 enzymes and underpinning critical processes such as cell division, DNA replication, and protein synthesis [11]. It is noteworthy that clinical concern typically revolves around Zn deficiency, which impairs growth, neurological development, and immunity, rather than toxicity from overexposure, which is rare [11]. Due to these exceptional

properties, biodegradable Mg-Zn alloys are considered a promising material for bone scaffold applications due to their combination of favorable mechanical properties, structural similarity to natural bone, and intrinsic degradability. This mechanical compatibility may help support physiological load transfer and reduce stress-shielding in potential implant applications.

A critical design parameter for bone scaffolds is their internal architecture. A high degree of interconnected porosity is essential to facilitate cell migration, vascularization, and bone ingrowth [12]. However, introducing porosity inherently compromises mechanical integrity [13]. One way to mitigate the effect of increased porosity and regain mechanical strength which could have been lost due to porosity is alloying. Again, Zn is particularly suitable for this purpose as it can enhance mechanical strength while maintaining biocompatibility [14]. Powder metallurgy using a space-holder technique is an effective method for producing porous Mg-Zn scaffolds with precise control over pore characteristics while minimizing matrix contamination [15].

While high porosity is often considered a desirable feature in porous scaffold design, its specific influence on the mechanical performance of low-temperature powder-metallurgy-fabricated Mg-Zn structures requires further investigation. The relationship between processing parameters, porous architecture, and resulting mechanical properties remains insufficiently understood. Therefore, this study focuses on the fabrication and mechanical characterization of porous Mg-Zn alloy scaffolds with approximately 40% to 70% porosity, produced via low-temperature powder metallurgy using carbamide as a space holder. The effects of porosity, zinc addition through comparison with literature, and sintering conditions on the microstructure, phase composition, and compressive properties of the scaffolds are systematically examined to establish structure-property relationships in porous Mg-Zn alloys.

2. Materials and method

2.1 Fabrication of porous Mg-Zn alloy scaffolds

Porous scaffolds were fabricated using commercial pure magnesium (Mg) and zinc (Zn) powders (purity >99.0 wt%, Nanjing Wanqing Chemical Glassware Instrument Co., Ltd, China). As shown in Figure 1, spherical carbamide ($(NH_2)_2CO$) particles, with a size range of 2.0 mm to 4.0 mm and a mean size of 3 mm, served as the space-holder agent. The scaffolds were consolidated via a low-temperature sintering process. Firstly, Mg and Zn powders in specific weight ratios were thoroughly blended using a mixer for 6 h. Subsequently, this metal powder mixture was combined with carbamide particles to form a uniform metal powder/carbamide mixture. The fabrication of green compacts was achieved through uniaxial compaction at a pressure of 300 MPa for 180 s, using a cylindrical steel die with a 25 mm internal diameter. The selected compaction pressure was intended to ensure adequate green strength without excessive densification, thereby helping to preserve the space-holder-derived porous scaffold structure [16]. Previous powder metallurgy studies have shown that compaction pressure strongly affects green density, pore formation, and sintering behavior [17].

The space-holder was subsequently removed via a two-stage process: first, a 6 h immersion in distilled water to dissolve the bulk of the carbamide, followed by a thermal treatment at 180°C for 2 h to eliminate any remnants. Sintering was conducted by individually wrapping the porous green compacts in aluminum foil, embedding them in a fine graphite powder bed (particle size ≤ 1 μm), and maintaining a temperature of 330°C for 12 h. After this thermal cycle, the scaffolds were cooled to ambient temperature.

2.2 Pore structure and composition characterization of porous Mg-Zn alloy scaffolds

The macro-structural parameters of pore size and porosity (Pr) were characterized for the fabricated scaffolds. The pore size was directly inherited from the carbamide space-holder, which had an initial size distribution of 2.0 mm to 4.0 mm. The porosity was determined using the following relationship:

$$\Pr\ (\%) = [(V - M/\rho_s) / \mathrm{V}] \times 100\% \qquad (1)$$

In this equation, V and M represent the geometric volume and mass of the scaffold, respectively, while ρ_s denotes the theoretical density of the Mg-Zn alloy. The value of ρ_s was derived from the rule of mixtures, assuming ideal densification of the metallic powders and a negligible influence from the sintering treatment.

The phase composition of the scaffolds cell walls was identified by X-ray diffraction (XRD, Rigaku SmartLab SE, Tokyo, Japan) with Cu-Kα radiation. For microstructural analysis, the foam samples were prepared through standard metallographic procedures of polishing and etching (using a solution of 5 mL acetic acid, 2.1 g picric acid, 5 mL water, and 35 mL ethanol). The microstructure and local chemical composition of the cell walls were then examined using scanning electron microscopy (SEM, CX200plus, COXEM Co., Ltd., Korea) coupled with energy-dispersive X-ray spectroscopy (EDS, Oxford, Bruker).

2.3 Microhardness and compression testing

The Mg-Zn scaffolds were prepared for microstructural analysis and hardness testing through a standard metallographic procedure. This involved progressive grinding with silicon carbide (SiC) paper up to 2000 mesh, followed by final polishing to a mirror finish on a velvet cloth with a diamond suspension using an automated polisher. The polished samples were then etched using a solution of acetic acid, picric acid, water, and ethanol. Vickers microhardness was measured with a digital tester (NXD-1000TC, Shanghai Taiming) using a 100 g load and a 15 s dwell time. To ensure accuracy, ten indentations were made on each specimen, and the results were averaged to report a representative hardness value.

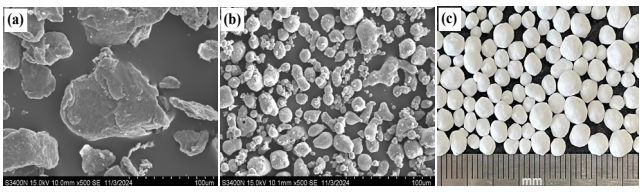

Figure 1. Scanning electron microscopy (SEM) images showing the morphology of the raw materials: (a) magnesium powder, (b) zinc powder, and (c) a macroscopic view of the carbamide space-holder granules.

The quasi-static compressive response was evaluated at ambient temperature on a universal testing machine (CMT4503, SUST Company, China) under a constant cross-head displacement rate of 2.0 mm·min^{-1}. The compression specimens were cylindrical with a diameter of 25 mm, and the height-to-diameter aspect ratios were approximately 0.50, 0.41, and 0.57 for Samples I, II, and III, respectively. Engineering stress (σ) was calculated by dividing the applied load by the original external cross-sectional area of the cylindrical specimen, $A_0=\pi(d/2)^2$, where "d" is the initial specimen diameter. Engineering strain (ε) was calculated from the displacement divided by the original specimen height. This method gives the nominal compressive stress, which is commonly used for reporting and comparing the compressive behavior of porous metallic scaffolds.

3. Results and discussion

3.1 Porosity and pore size evaluation of porous Mg-Zn alloy scaffolds

The fabricated Mg-Zn scaffolds irrespective of porosity exhibited a heterogeneous porous microstructure. As a reference, one sample with approximately 60% porosity containing 41 open pores is shown in Figure 2(a). The surface was analyzed using ImageJ software for pore size and morphology evaluation. Open pores were defined as pores that are exposed and connected to the external surface of the specimen, which can be directly observed and quantified from surface micrographs using ImageJ analysis. The number of open pores was determined by counting the surface-exposed pores from the analyzed micrograph after image thresholding and segmentation in ImageJ. Individual pores were characterized using the geometric mean of their minor and major diameters, providing an effective measure of each pore's size. The overall mean pore size of the scaffold, calculated as the arithmetic mean of the individual geometric mean, was 3.02 ± 0.8 mm, with a standard deviation of 0.80 mm. Individual pore diameters ranged from 1.26 mm to 4.76 mm, while the average aspect ratio (a/b) was 0.839, indicating that the pores are generally near-spherical to slightly elongated. This pore architecture is expected to provide a balance between mechanical integrity and porosity.

Although this study primarily focuses on mechanical characterization, the observed pore morphology may be favorable for processes such as fluid transport and potential cell migration within a scaffold. The pores, with an approximate diameter of 3 mm and a hierarchical distribution, form a well-connected porous network, as highlighted by the marked white arrows in Figure 2(a). This architecture could influence the movement of fluids and solutes through the scaffold and may also affect degradation kinetics and ion exchange under physiological conditions. The combination of interconnected porosity and moderate size variability provides a structural framework that supports uniform load distribution and could contribute to controlled material dissolution in future biological studies.

3.2 SEM/EDS analysis of porous Mg-Zn alloy scaffolds

The microstructural and compositional features of the fabricated porous Mg–Zn scaffold, sintered at 330°C for 12 h, were analyzed using scanning electron microscopy (SEM) coupled with energy-dispersive X-ray spectroscopy (EDS). The EDS results provided the elemental distribution of magnesium (Mg) and zinc (Zn) at selected regions in Figure 3, as summarized in Table 1. The data indicate distinct compositional variations across the examined points (A–G), reflecting the coexistence of multiple phases within the alloy matrix.

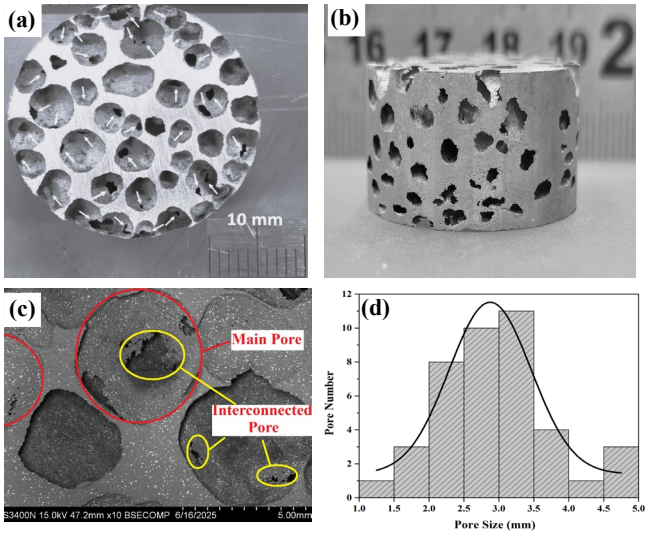

Figure 2. Morphological analysis of the porous Mg-Zn scaffold. (a,b) Cross-sectional optical images showing the porous structure. White arrows in (a) and yellow circles in (c) indicate interconnected pores. (d) Histogram quantifying the pore size distribution corresponding to sample (a).

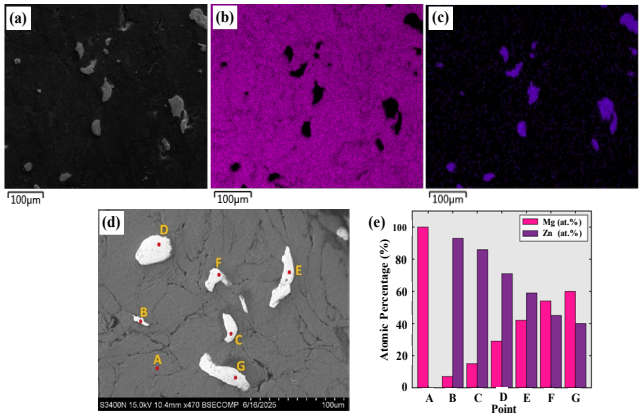

Figure 3. Compositional analysis of the porous Mg-Zn scaffold. (a,b,c) EDS elemental mapping of cell wall of porous Mg-Zn scaffold. (d) Backscattered electron SEM image of the Mg-10 wt% Zn alloy cell wall, showing phase contrast between the matrix and intermetallic compounds. (e) Elemental atomic % at different points of the cell wall of the Mg-10 wt% Zn scaffold, as marked in (d).

Table 1. EDS analysis of the marked points in Figure 3(d) and possible metallic phases.

Point	Mg [at%]	Zn [at%]	Associated phase
A	100	0	Pure Mg particle
B	7.69	92.33	Zn-rich particle
C	14.87	85.13	Close to Mg_2Zn_{11}
D	29.28	70.72	$MgZn_2$
E	41.53	58.47	Approaching $MgZn_2$
F	54.44	45.56	α-Mg + $MgZn_2$ diffusion zone
G	60.36	39.64	α-Mg + $MgZn_2$ diffusion zone

The EDS spectra revealed that Point A corresponds to nearly pure magnesium, indicating the presence of unreacted Mg particles retained within the porous matrix. Point B exhibited a markedly high Zn concentration, suggesting the formation of Zn-rich particles or segregated Zn regions, possibly resulting from partial elemental diffusion during sintering. The composition recorded at Point C closely resembles the stoichiometry of the Mg_2Zn_{11} intermetallic compound, which has been widely reported as a stable Zn-rich phase in Mg-Zn binary systems [18]. Point D is consistent with the stoichiometry of $MgZn_2$, a C14-type Laves intermetallic phase frequently observed in Mg-Zn alloys at intermediate Zn contents [19]. This phase often precipitates along particle boundaries or within the diffusion layer, contributing to the alloy's mechanical reinforcement. Point E, with a slightly higher Mg content, appears to represent a transitional region approaching the Mg-rich side of the intermetallic regime, implying partial diffusion of Mg and Zn-rich interfusion domains during thermal processing.

Points F and G lie within the compositional range of the α-Mg solid solution, yet with significant Zn enrichment. These points correspond to the α-Mg + $MgZn_2$ diffusion zone, formed through mutual diffusion of Mg and Zn during sintering. The formation of such graded microstructures suggests strong elemental interdiffusion, leading to the development of intermetallic layers and heterogeneous grain regions within the scaffold. The presence of $MgZn_2$ and Mg_2Zn_{11} intermetallics, together with α-Mg diffusion regions, is consistent with the equilibrium phase relations in the Mg-Zn system reported in earlier studies [20–22].

The overall compositional trends and corresponding phase identification confirm the multiphase nature of the porous Mg-Zn scaffold, comprising unreacted Mg, Zn-rich inclusions, and stable intermetallic compounds such as $MgZn_2$ and Mg_2Zn_{11}, along with diffusion zones between α-Mg and $MgZn_2$. This microstructural heterogeneity is expected to influence the mechanical behavior of the scaffold through local strengthening effects and the formation of intermetallic phases. The presence of these phases may also affect the degradation behavior of Mg-Zn alloys, as reported in previous studies [23,24].

3.3 Effect of zinc alloying on Mg-Zn alloy scaffolds

Backscattered electron images (BSEIs) of the porous Mg-Zn alloy scaffold cell walls at different magnifications are presented in Figure 5(a,b). Bright contrast phases are visible within the cell walls. As confirmed by EDS analysis, these phases consist of Mg and Zn, with atomic ratios approximating the stoichiometric compositions of $MgZn_2$ and Mg_2Zn_{11}. This confirms the formation of Mg-Zn intermetallic compounds during the 330°C, 12 h sintering treatment.

Minor deviations, including α-Mg + $MgZn_2$ Diffusion Zone and Zn-rich areas, likely arise from local variations in elemental diffusion and the particle size of the starting powders, which can limit reaction completeness during sintering [25,26]. Moreover, analysis as shown in Figure 4 revealed multiple phases were primarily identified in the patterns including α-Mg, $MgZn_2$, Mg_2Zn_{11}, and Zinc rich phase, when analyzed using JADE Software. The diffraction pattern confirmed the presence of hexagonal α-Mg as the dominant phase, evidenced by characteristic peaks at 32.2°, 34.4°, and 36.6°. More significantly, the detection of peaks at 36.3°, 43.3°, and 68.6° confirms the presence of Zn rich phases and formation of MgZn intermetallic compounds.

These peaks exhibit excellent agreement with reference patterns, with angular deviations within ± 0.1°, demonstrating high reliability in phase identification. Both XRD and EDS point analysis identified α-Mg and $MgZn_2$ as the primary crystalline phases, while revealing some localized regions with composition approaching Mg_2Zn_{11} stoichiometry.

To further quantify the effect of the 10 wt% Zn addition, the intermetallic phases in the SEM image of Figure 5(b) were analyzed using ImageJ software. The results, summarized in Figure 5(c), include the number of intermetallic grains (N), their total area (Sb), the total cell wall area (Sc), and their ratio (Sb/Sc). Furthermore, the grain size distribution and number density, presented in the histogram in Figure 5(d), demonstrate that the majority (>65%) of the Mg-Zn intermetallics have a grain size between 0.002 mm and 0.014 mm. A significant microstructural hierarchy was observed between SEM and XRD analyses. While SEM revealed $MgZn_2$ intermetallic grains ranging from 2 μm to 14 μm, XRD crystallite size analysis indicated much finer domains of ~40 nm. This discrepancy suggests that each visible intermetallic grain by SEM consists of numerous nanocrystalline subdomains, creating a hierarchical microstructure that may enhance mechanical properties through boundary strengthening. In addition, despite porosities of 40.65%, 60.38%, and 68.70%, all Mg-Zn alloy scaffolds exhibited a constant Mg-Zn intermetallic area fraction of 5.20%, resulting from the fixed 10 wt% Zn addition.

The integration of 10 wt% zinc into magnesium scaffolds creates a material with a compelling profile for bone repair, successfully balancing mechanical integrity with biological function. Zinc enhances the magnesium matrix through solid-solution strengthening, while the consequent formation of MgZn intermetallic phases along the scaffold's cell walls provides critical reinforcement, boosting its resistance to deformation under load [27]. During degradation, Zn^{2+} ions may be released from the scaffold, which in other studies have been reported to influence bone-forming cells and mineralization [28]. Thus, the Mg-10Zn scaffold's mechanically robust, hierarchical porous structure provides structural stability and controlled degradation, potentially supporting future biological applications. These properties suggest that the scaffold could be considered for load-bearing applications, subject to further biological evaluation.

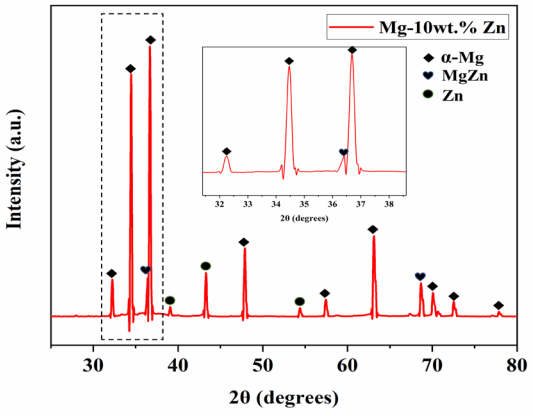

Figure 4. XRD pattern of the porous Mg-10 wt% Zn scaffold cell walls.

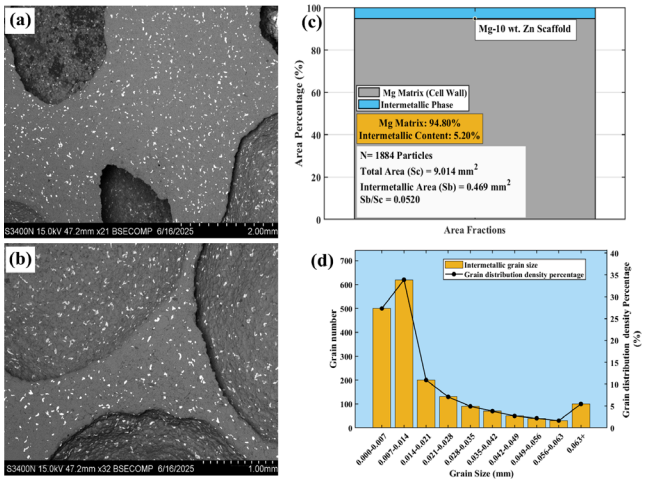

Figure 5. (a,b) Backscattered SEM images of porous Mg-Zn scaffold at at different resolutions, (c) grain size distribution and density of intermetallic phases, analyzed from image (b), and (d) quantitative intermetallic phase content measured from the area in image (b).

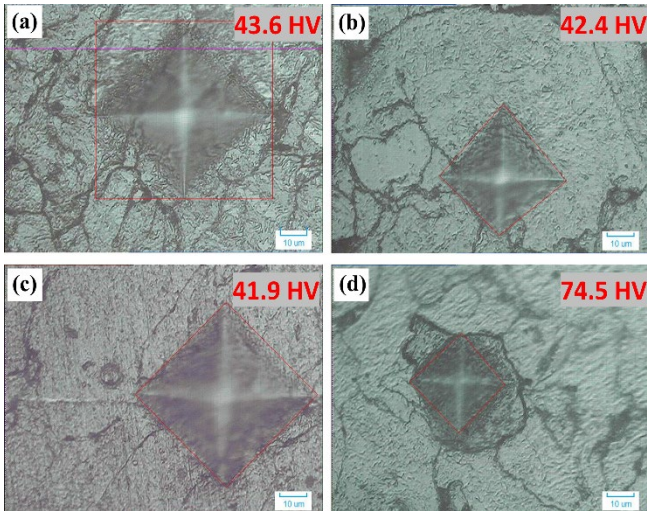

Figure 6. Microhardness of (a) Sample I, (b) Sample II, (c) Sample III, and (d) microhardness at a possible Mg/Zn intermetallic region in the cell wall of Sample II.

3.4 Surface hardness of Mg-Zn alloy scaffolds

The Vickers microhardness of the scaffold struts, indicative of the local mechanical properties of the constituent material, was evaluated across all sample groups. The results revealed that elevating the porosity from 40.65 ± 3.04% to 68.70 ± 0.95 % did not induce a statistically significant variation in the microhardness. The mean values remained consistent at approximately 42.3 ± 3.0 HV, indicating that unlike compressive strength, the global architectural parameter of porosity exerts a negligible influence on this localized hardness property. Remarkably, the hardness values of Mg 10 wt% Zn scaffolds are within the range of human bone's hardness (40 HV to 79 HV) [29,30].

This observed invariance can be rationalized by considering the intrinsic nature of the micro indentation technique. The test probes a micron-scale volume on the surface of the individual struts, a scale orders of magnitude smaller than that of the macro-pores. Consequently, the measured hardness is a function solely of the local microstructure and composition of the solid matrix material, independent of the scaffold's overall porous architecture. The variability at different points, evidenced by the Figure 5, is attributed to microstructural heterogeneity at the indentation site. As corroborated by EDS elemental mapping and XRD analysis (Section 3.2), the strut surface comprises a multi-phase microstructure including a primary α-Mg phase, Zn in solid solution, and discrete Mg-Zn intermetallic precipitates. Given the finite size of the indenter, measurements inherently sample these distinct regions. As an impression falling upon a hard intermetallic particle will yield a higher hardness value than one confined to the softer magnesium matrix as shown in Figure 6. This phenomenon is responsible for the data dispersion observed within each sample group.

3.5 Compressive behavior of porous Mg-Zn alloy scaffolds

Representative compressive stress-strain curves for the fabricated Mg-10 wt% Zn scaffolds are depicted in Figure 7(d), illustrating the mechanical behavior at porosities of 39.25 ± 1.06%, 60.38 ± 1.03%, and 68.7 ± 0.95%. All curves exhibit three characteristic deformation regions, (i) a linear elastic region, where stress increases proportionally with strain until reaching the compressive strength; (ii) a plateau region, initiated by a stress drop from yielding and crack formation, and characterized by subsequent stress oscillations, and (iii) a final densification region [2]. Since all scaffolds in the present study contained a constant zinc composition, no direct comparison was made regarding the effect of Zn content on mechanical strength. However, comparison with previous studies suggests that Zn addition can enhance the strength of Mg-based porous scaffolds. The sintering process promotes reaction between Zn and Mg, resulting in metallurgical bonding and the formation of intermetallic compounds [31], as evidenced by EDS and XRD analysis. These intermetallics act as reinforcing phases within the cell walls, thereby increasing the mechanical strength of the porous Mg-Zn alloys compared to porous Mg [32].

The compressive strength of the porous Mg-10Zn scaffolds was systematically evaluated, revealing a definitive correlation with architectural porosity that aligns with the fundamental principles of the Ashby-Gibson model for cellular solids. Beginning with the densest structures, Sample I scaffolds, characterized by a low porosity of 40.65 ± 3.04%, demonstrated a high mean compressive strength of 20.11 ± 0.40 MPa. This robust performance is a direct consequence of a substantial volume fraction of solid material, resulting in thick, well-connected cell walls that can effectively bear and transfer applied loads, a hallmark of low-porosity cellular materials. A moderate increase in porosity to 60.38 ± 1.03% in Sample II scaffolds resulted in a predictable decrease in strength to 6.64 ± 0.24 MPa, consistent with the model's prediction that mechanical properties scale with the relative density raised to a power. This reduction occurs because increasing porosity directly decreases the effective load-bearing cross-sectional area of the solid matrix, making the structure more susceptible to buckling and fracture.

Progressing to the most porous structures, Sample III scaffolds with a high porosity of 68.70 ± 0.95% exhibited a mean compressive strength of 3.81 ± 0.45 MPa. Critically, even at this elevated porosity level, the compressive strength and Young's modulus remain within the reported range for human cancellous bone (2 MPa to 12 MPa and 0.01 GPa to 2 GPa) [33,34] , underscoring the biomimetic potential of these constructs. The observed exponential decay in strength from

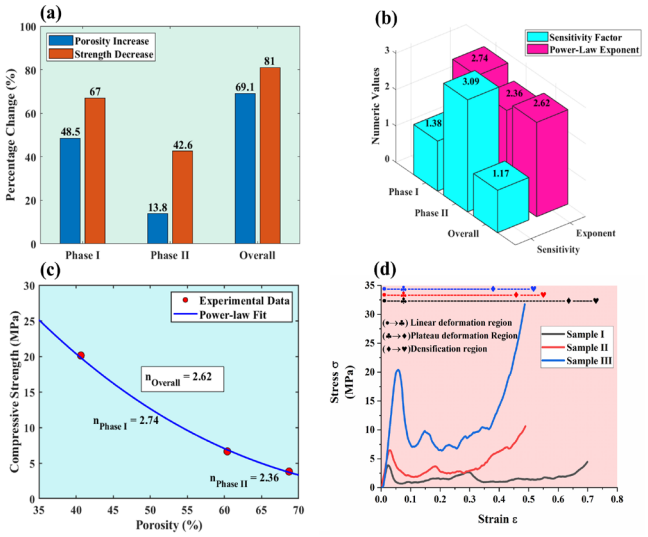

Figure 7. Compressive behavior of porous Mg 10 wt% Zn scaffolds fabricated via powder metallurgy. (a) Percentage variation in porosity and strength, (b) sensitivity factor and power-law exponent from the porosity—strength relation, (c) experimental data fitted to the Gibson-Ashby model (n(Phase I) = 2.74, n(Phase II) = 2.36 n(Overall) = 2.62), and (d) compressive stress-strain curves showing linear, plateau, and densification regions.

Sample I to Sample III, a 81.0 % decrease corresponding to a 69.1% increase in porosity is a classic manifestation of the Ashby-Gibson relationship, where the mechanical properties of a porous solid are primarily governed by the bending and buckling of its thinning struts. The excellent consistency in mechanical properties within each batch indicates a highly reproducible fabrication process. When connected to previous findings on microhardness, which showed a significant increase post-sintering due to intermetallic formation, it is evident that the intrinsic strength of the Mg-Zn matrix provides a strong foundation, while the macro-architectural porosity dictates the final, tailorable mechanical performance of the scaffold. This allows for the design of scaffolds that can mimic either strong cortical bone or more compliant cancellous bone by simply controlling the pore volume. Table 2 presents all the mechanical properties of Mg-Zn scaffolds produced in this study.

The quantitative analysis of the porosity-strength relationship reveals critical non-linear behavior with significant implications for scaffold design. The progression from low (40.65%) to high (68.70%) porosity was marked by a dramatically increasing sensitivity of compressive strength to porosity changes. Specifically, an initial 48.6% increase in porosity (Sample I to II, termed as phase I) resulted in a 67.0% loss of strength, while a subsequent, smaller 13.8% porosity increase (Sample II to III, termed as phase II) still induced a substantial 42.6% reduction in load-bearing capacity. This escalating effect was evidenced by a sensitivity factor that quantifies how much the compressive strength decreases (%) per percent increase in porosity, calculated using Equation (2):

$$S = (\Delta\sigma/\sigma_0)/(\Delta P/P_0) \quad (2)$$

Where S is sensitivity factor, σ_0 and σ is compressive strength of lower (P_0) and higher porosity (P) samples respectively. Whereas, $\Delta\sigma$ and ΔP shows change in compressive strength = $\sigma_0 - \sigma$ and change in porosity = $P - P_0$, respectively.

Table 2. Mechanical properties of porous Mg-10Zn scaffolds produced in current study.

Sample batch	Targeted porosity [%]	Measured porosity [%]	Compressive strength [MPa]	Young's modulus [GPa]	Yield strength [MPa]	Plateau stress [MPa]	Energy absorption [MJ·m^{-3}]
Sample I	40	40.65 ± 3.04	20.11 ± 0.40	0.402 ± 0.025	18.50 ± 0.10	9.14 ± 1.08	4.53 ± 0.28
Sample II	60	60.38 ± 1.03	6.64 ± 0.24	0.211 ± 0.032	6.05 ± 0.17	2.60 ± 0.25	1.142 ± 0.204
Sample III	70	68.70 ± 0.95	3.81 ± 0.45	0.229 ± 0.030	3.58 ± 0.36	1.32 ± 0.21	0.861 ± 0.133

Table 3. Compressive strengths of porous Mg/Mg alloy scaffolds as reported in the literature.

Matrix metal	Fabrication method	Temperature [°C]	Porosity [%]	Compressive strength [MPa]	Reference
Pure Mg	Replication method	750	67	2.5	[39]
Pure Mg	Melt infiltration method	680	54.4 to70.4	8.65 to 3.67	[40]
Mg 6 wt% Zn	Melt infiltration method	550	52.2	8.6	[41]
Pure Mg	Space holder powder metallurgy	630	62.4	0.7 ± 0.2	[42]
ZWM200	Melt infiltration method	755	30 to 69	12.15 to 2.31	[43]
Mg	Ti wire space holder method	700	43.5 to 54.2	6.2 to 4.3	[44]
Pure Mg	Space holder powder metallurgy method	560 to 650	60	7	[45]
Pure Mg	Mg scaffold by Aida *et al.* 630°C for 2.5 h	630	64.7	5	[46]
Pure Mg	Space holder powder metallurgy method	580 to 630	65	4.48 to 6.00	[47]
Mg 10 wt% Zn	Space holder powder metallurgy method	330	40.65 to 68.7	20.11 to 3.81	This study

The sensitivity factor rises from 1.38 to 3.09 across phase I to phase II as shown in Figure 7(b), underscores an exponential decay pattern and identifies a critical threshold above approximately 60% porosity. Beyond this point, the scaffold's mechanical integrity becomes exceptionally sensitive to architectural variations, where minimal increases in pore volume precipitate disproportionate declines in strength, likely due to the transition of the dominant deformation mechanism to the buckling of critically thin struts. These findings highlight that while tailoring porosity is an effective strategy for achieving biomimetic properties, precise control is paramount, especially for high-porosity scaffolds targeting cancellous bone applications, as minor architectural fluctuations can significantly compromise mechanical performance.

Furthermore, The relationship between compressive strength and relative density was evaluated based on the Gibson-Ashby model for open-cell metallic foams [35,36], which expresses the dependence of strength on density as:

$$\sigma^*/\sigma_s = C_\sigma\left(\rho^*/\rho_s\right)^n \quad (3)$$

where σ* and σs are the compressive strengths of the porous and fully dense Mg-10 wt% Zn alloy scaffold. Whereas ρ^*/ρ_s is relative density of porous Mg-10 wt% Zn scaffold. For the present Mg-10Zn scaffolds, the experimental data were fitted using the equivalent empirical relation:

$$\sigma = A(1-P)^n \quad (4)$$

where A and n were determined by linear regression of ln(σ) vs. ln(1 − P), and P is the porosity expressed as a fraction. The least-squares regression of compressive strength versus relative density yielded a power-law exponent of $n = 2.62 \pm 0.10$ ($R^2 = 0.9985$) as shown in Figure 7(c), consistent with strong scaling behavior. The prefactor was $A = 77.6$, giving the fitted relationship $\sigma = 77.6\ (1-P)^{2.62}$, which is higher than the theoretical value of $n = 1.5$ predicted by the Ashby-Gibson model for ideal open-cell foams. This elevated exponent indicates that the compressive strength of the Mg-10Zn scaffolds decreases more rapidly with porosity than in an idealized cellular solid. The deviation is attributed to microstructural imperfections within the scaffold struts that are not accounted for in the theoretical model. Specifically, defects such as micro-porosity and microcracks, introduced during the powder metallurgy and sintering process, act as stress concentrators and reduce the intrinsic strength of the solid phase. As porosity increases and the struts become progressively thinner, these imperfections amplify the susceptibility to brittle fracture and localized buckling. Consequently, the measured exponent exceeds the ideal value, reflecting the combined effect of geometric thinning and defect-driven weakening of the scaffold architecture [37,38].

Table 3 compares the compressive strengths of porous Mg-Zn scaffolds from this study with literature values. The results demonstrate that the Mg-Zn scaffolds fabricated here exhibit mechanical properties comparable to those produced by high-temperature methods, including replication, melt infiltration, and space-holder powder metallurgy. Furthermore, this study indicates that porous Mg-Zn alloys can achieve competitive compressive strength through low-temperature sintering in a space-holder powder metallurgy process.

4. Conclusions

Porous Mg-10 wt% Zn scaffolds with porosities of 40.65%, 60.38%, and 68.7% were successfully fabricated via powder metallurgy using carbamide granules as a space-holder. The processing route produced well-distributed, interconnected pores and metallurgically bonded cell walls, confirming the effectiveness of carbamide in generating controlled porosity. Following are the main conclusions:

Mechanical characterization revealed a clear density-dependent response consistent with Gibson-Ashby scaling behavior. The compressive strength decreased from 20.11 ± 0.40 MPa at 40.65 ± 3.04% porosity to 3.81 ± 0.45 MPa at 68.70 ± 0.95% porosity, while Young's modulus declined from 0.402 ± 0.025 GPa to 0.229 ± 0.030 GPa. The plateau stress and energy absorption similarly diminished with increasing porosity, reflecting the reduction in load-bearing cross-section and enhanced pore connectivity.

The microhardness remained nearly constant at around 42 HV across all porosity levels, suggesting that the intrinsic hardness of the Mg-10Zn alloy matrix was unaffected by porosity variation and that deformation behavior was primarily governed by the porous architecture rather than by compositional or phase changes.

The compressive properties, including compressive strength and Young's modulus, are within the range reported for human cancellous bone, indicating that the scaffolds achieve mechanical characteristics relevant for potential load-bearing applications.

Collectively, these findings demonstrate that the Mg-10 wt% Zn system, processed through the carbamide-based space-holder technique, provides tunable porosity and predictable mechanical performance. These results provide a foundation for future investigations that could evaluate degradation behavior and biological responses under physiological conditions.

Declaration of competing interest

The authors declare that they have no known competing financial interests or personal relationships that could have appeared to influence the work reported in this paper.

Acknowledgements

This work was supported by the National Natural Science Foundation of China (Nos. 52474388, 12072105, 11932006)

References

[1] Y. Liu, L. He, L. Cheng, X. Li, M. Gao, Q. Li, J. Gao, and M. Ramalingam, "Enhancing bone grafting outcomes: A comprehensive review of antibacterial artificial composite bone scaffolds," *Medical Science Monitor*, vol. 29, p. e939972, 2023.

[2] S. Singhawannurat, P. Lawtae, C. Rojviriya, and C. Phoovasawat, "Development of PLA/HA porous scaffolds with controlled pore sizes using the combined freeze drying and sucrose leaching technique for bone tissue engineering," *Journal of Metals, Materials and Minerals*, vol. 34, no. 2, p. 1928, 2024.

[3] D. B. Burr, "Bone morphology and organization," *in Basic and Applied Bone Biology*, Elsevier, 2019, pp. 3–26.

[4] M. F. S. F. de Moura, and N. Dourado, "*Fracture and fatigue characterisation of cortical bone tissue*," Boca Raton: CRC Press, 2024.

[5] P. Baskaran, B. Muthiah, and V. Uthirapathy, "A systematic review on biomaterials and their recent progress in biomedical applications: bone tissue engineering," *Reviews in Inorganic Chemistry*, vol. 45, no. 4, pp. 747–781, 2025.

[6] H. Shao, K. Wen, R. Liu, N. Ding, Y. Gong, Y. Zhuang, and Y. He, "3D Printing of Bioceramic Multifunctional Scaffolds for Bone Tissue Engineering," A*dvanced Functional Materials*, vol. 35, no. 49, 2025.

[7] X. Gu, Y. Zheng, Y. Cheng, S. Zhong, and T. Xi, "In vitro corrosion and biocompatibility of binary magnesium alloys," *Biomaterials*, vol. 30, no. 4, pp. 484–498, 2009.

[8] F. Witte, V. Kaese, H. Haferkamp, E. Switzer, A. Meyer-Lindenberg, C. J. Wirth, and H. Windhagen, "In vivo corrosion of four magnesium alloys and the associated bone response," Biomaterials, vol. 26, no. 17, pp. 3557–3563, 2005.

[9] G. Song, "Control of biodegradation of biocompatable magnesium alloys," *Corrosion Science*, vol. 49, no. 4, pp. 1696–1701, 2007.

[10] B. Homayun, and A. Afshar, "Microstructure, mechanical properties, corrosion behavior and cytotoxicity of Mg–Zn–Al–Ca alloys as biodegradable materials," *Journal of Alloys and Compounds*, vol. 607, pp. 1–10, 2014.

[11] L. M. Plum, L. Rink, and H. Haase, "The essential toxin: Impact of zinc on human health," *International Journal of Environmental Research and Public Health*, vol. 7, no. 4, pp. 1342–1365, 2010.

[12] A. Cheng, Z. Schwartz, A. Kahn, X. Li, Z. Shao, M. Sun, Y. Ao, B. D. Boyan, and H. Chen, "Advances in porous scaffold design for bone and cartilage tissue engineering and regeneration," *Tissue Engineering Part B: Reviews*, vol. 25, no. 1, pp. 14–29, 2019.

[13] G. Hannink, and J. J. C. Arts, "Bioresorbability, porosity and mechanical strength of bone substitutes: What is optimal for bone regeneration?," *Injury*, vol. 42, pp. S22–S25, 2011.

[14] Y. Hu, X. Guo, Y. Qiao, X. Wang, and Q. Lin, "Preparation of medical Mg–Zn alloys and the effect of different zinc contents on the alloy," *Journal of Materials Science: Materials in Medicine*, vol. 33, no. 1, p. 9, 2022.

[15] B. Arifvianto, and J. Zhou, "Fabrication of metallic biomedical scaffolds with the space holder method: A review," *Materials*, vol. 7, no. 5, pp. 3588–3622, 2014.

[16] S. Sathaiah, L. Singh, N. R. Gorhe, T. C. Joshi, A. Pandey, A. N. Ch. Venkat, G. K. Gupta, L. M. Joshi, K. K. Saxena, and D. P. Mondal, "Effect of compaction pressure on microstructural, mechanical, and thermal properties of aluminum foams processed through space-holder technique," *Journal of Materials Engineering and Performance*, vol. 34, no. 1–2, pp. 6351–6361, 2025.

[17] V. Moeun, and S. Asavavisithchai, "Effect of compaction pressure on the structure and mechanical properties of functionally graded aluminium-glass microsphere (FGAGM) foams produced by powder metallurgy process," *Journal of Metals, Materials and Minerals*, vol. 35, no. 4, p. e2432, 2025.

[18] P. Jiang, C. Blawert, and M. L. Zheludkevich, "The corrosion performance and mechanical properties of Mg-Zn based alloys—A review," *Corrosion and Materials Degradation*, vol. 1, no. 1, pp. 92–158, 2020.

[19] F. Stein, and A. Leineweber, "Laves phases: A review of their functional and structural applications and an improved fundamental understanding of stability and properties," *Journal of Materials Science*, vol. 56, no. 9, pp. 5321–5427, 2021.

[20] J. Dong, P. Lin, N. E. Putra, N. Tumer, M. A. Leeflang, Z. Huan, L. E. Fratila-Apachitei, J. Chang, A. A. Zadpoor, and J. Zhou, "Extrusion-based additive manufacturing of Mg-Zn/bioceramic composite scaffolds," *Acta Biomaterialia*, vol. 151, pp. 628–646, 2022.

[21] A. Mostafa, and M. Medraj, "Phase equilibria of the Ce-Mg-Zn ternary system at 300°C," *Metals*, vol. 4, no. 2, pp. 168–195, 2014.

[22] C. C. Kammerer, N. S. Kulkarni, R. J. Warmack, and Y. H. Sohn, "Interdiffusion and impurity diffusion in polycrystalline Mg solid solution with Al or Zn," *Journal of Alloys and Compounds*, vol. 617, pp. 968–974, 2014.

[23] M. A. F. Romzi, J. Alias, and M. I. M. Ramli, "Effect of zinc (Zn) on the microstructure and corrosion behaviour of magnesium (Mg)," *Materials Today: Proceedings*, vol. 48, pp. 1873–1879, 2022.

[24] J. M. Byun, J. M. Yu, D. K. Kim, T.-Y. Kim, W.-S. Jung, and Y. Do Kim, "Corrosion behavior of Mg_2Zn_{11} and $MgZn_2$ single phases," *Korean Journal of Metals and Materials*, vol. 51, no. 6, pp. 413–419, 2013.

[25] M. Valant, D. Suvorov, R. C. Pullar, K. Sarma, and N. McN. Alford, "A mechanism for low-temperature sintering," *Journal of the European Ceramic Society*, vol. 26, no. 13, pp. 2777–2783, 2006.

[26] Z. Chen, T. Takeda, and K. Ikeda, "Microstructural evolution of reactive-sintered aluminum matrix composites," *Composites Science and Technology*, vol. 68, no. 10–11, pp. 2245–2253, 2008.

[27] T. N. Saraçoğlu, S. Polat, E. Koç, M. Mashrah, A. Najah Saud, and M. Michalska-Domańska, "Investigating the oxidation behavior of Mg-Zn alloy: Effects of heating rates, gas flow, protective atmosphere, and alloy composition," *Journal of Metals, Materials and Minerals*, vol. 34, no. 3, p. 2033, 2024.

[28] H. Yang, B. Jia, Z. Zhang, X. Qu, G. Li, W. Lin, D. Zhu, K. Dai, and Y. Zheng, "Alloying design of biodegradable zinc as promising bone implants for load-bearing applications," *Nature Communications*, vol. 11, no. 1, p. 401, 2020.

[29] S. Wu, X. Liu, K. W. K. Yeung, C. Liu, and X. Yang, "Biomimetic porous scaffolds for bone tissue engineering," *Materials Science and Engineering: R: Reports*, vol. 80, pp. 1–36, 2014.

[30] X. Wang, S. Xu, S. Zhou, W. Xu, M. Leary, P. Choong, M. Qian, M. Brandt, and Y. M. Xie, "Topological design and additive manufacturing of porous metals for bone scaffolds and orthopaedic implants: A review," *Biomaterials*, vol. 83, pp. 127–141, 2016.

[31] S. Teslia, M. Kovalenko, M. Teslia, M. Vterkovskiy, I. Solodkyi, P. Loboda, and T. Soloviova, "The activation of magnesium sintering by zinc addition," *Alloys*, vol. 3, no. 3, pp. 178–189, 2024.

[32] Z. S. Seyedraoufi, and Sh. Mirdamadi, "Synthesis, microstructure and mechanical properties of porous Mg Zn scaffolds," *Journal*

of the Mechanical Behavior of Biomedical Materials, vol. 21, pp. 1–8, 2013.

[33] Q. Fu, E. Saiz, M. N. Rahaman, and A. P. Tomsia, "Toward strong and tough glass and ceramic scaffolds for bone repair," *Advanced Functional Materials*, vol. 23, no. 44, pp. 5461–5476, 2013.

[34] L. J. Gibson, "The mechanical behaviour of cancellous bone," *Journal of Biomechanics*, vol. 18, no. 5, pp. 317–328, 1985.

[35] B. Parveez, N. A. Jamal, H. Anuar, Y. Ahmad, A. Aabid, and M. Baig, "Microstructure and mechanical properties of metal foams fabricated via melt foaming and powder metallurgy technique: A review," *Materials*, vol. 15, no. 15, p. 5302, 2022.

[36] L. J. Gibson, and M. F. Ashby, "Material properties," in *Cellular Solids Structure and Properties*, Cambridge University Press, 1997, pp. 52–92.

[37] G. Luo, Y. Zhu, R. Zhang, C. Peng, Q. Liu, J. Zhang, Y. San, H. Yuan, W. Guo, Q. Shen, and L. Zhang, "A review on mechanical models for cellular media: Investigation on material characterization and numerical simulation," *Polymers*, vol. 13, no. 19, p. 3283, 2021.

[38] K. Ćwieka, and J. Skibiński, "Elastic properties of open cell metallic foams—modeling of pore size variation effect," *Materials*, vol. 15, no. 19, p. 6818, 2022.

[39] J. O. Osorio-Hernández, M. A. Suarez, R. Goodall, G. A. Lara-Rodriguez, I. Alfonso, and I. A. Figueroa, "Manufacturing of open-cell Mg foams by replication process and mechanical properties," *Materials & Design*, vol. 64, pp. 136–141, 2014.

[40] X. Wang, Z. Li, Y. Huang, K. Wang, X. Wang, and F. Han, "Processing of magnesium foams by weakly corrosive and highly flexible space holder materials," *Materials & Design*, vol. 64, pp. 324–329, 2014.

[41] Y. Yan, Y. Kang, D. Li, K. Yu, T. Xiao, Q. Wang, Y. Deng, H. Fang, D. Jiang, and Y. Zhang, "Microstructure, mechanical properties and corrosion behavior of porous Mg-6 wt% Zn Scaffolds for bone tissue engineering," *Journal of Materials Engineering and Performance*, vol. 27, no. 3, pp. 970–984, 2018.

[42] N. Zou, and Q. Li, "Mechanical properties of lightweight porous magnesium processed through powder metallurgy," *JOM*, vol. 70, no. 5, pp. 650–655, 2018.

[43] J. Trinidad, I. Marco, Q. Arruebarrena, J. Wendt, D. Letzig, E. S. de Argandona, and R. Goodall, "Processing of magnesium porous structures by infiltration casting for biomedical applications," *Advanced Engineering Materials*, vol. 16, no. 2, pp. 241–247, 2014.

[44] G. Jiang, and G. He, "A new approach to the fabrication of porous magnesium with well-controlled 3D pore structure for orthopedic applications," *Materials Science and Engineering C*, vol. 43, pp. 317–320, 2014.

[45] G. L. Hao, F. S. Han, and W. D. Li, "Processing and mechanical properties of magnesium foams," *Journal of Porous Materials*, vol. 16, no. 3, pp. 251–256, 2009.

[46] S. F. Aida, H. Zuhailawati, and A. S. Anasyida, "The Effect of space holder content and sintering temperature of magnesium foam on microstructural and properties prepared by sintering dissolution process (SDP) using carbamide space holder," *Procedia Engineering*, vol. 184, pp. 290–297, 2017.

[47] S. Toghyani, and M. Khodaei, "Modified spacer removal and optimum sintering temperature for porous magnesium scaffold fabrication," *Journal of Tissue and Materials*, vol. 2, pp. 48–57, 2019.